Surface wave propagation control with locally resonant metasurfaces using topology-optimized resonators

Daniel Giraldo Guzman,¹ Lalith Sai Srinivas Pillarisetti,² Mary Frecker,¹ Cliff J. Lissenden,² and Parisa Shokouhi,²

This paper is part of a special issue on Wave phenomena in periodic, near-periodic, and locally resonant systems

Locally resonant elastodynamic metasurfaces for suppressing surface waves have gained popularity in recent years, especially due to their potential in low-frequency applications, such as seismic barriers. Their design strategy typically involves tailoring geometrical features of local resonators to attain a desired frequency bandgap through extensive dispersion analyses. In this paper, we present a systematic design methodology to conceive these local resonators using topology optimization, where frequency bandgaps develop by matching multiple antiresonances with predefined target frequencies. Our design approach modifies an individual resonator's response to unidirectional harmonic excitations in the in-plane and out-of-plane directions, mimicking the elliptical motion of surface waves. Once an arrangement of optimized resonators composes a locally resonant metasurface, frequency bandgaps appear around the designed antiresonance frequencies. Numerical investigations analyze three case studies showing that longitudinal-like and flexural-like antiresonances lead to nonoverlapping bandgaps unless both antiresonance modes are combined to generate a single and wider bandgap. Experimental data demonstrate good agreement with the numerical results, validating the proposed design methodology as an effective tool to realize locally resonant metasurfaces by

matching multiple antiresonances such that bandgaps generated due to in-plane and out-of-plane

surface wave motion combine into wider bandgaps.

¹ Department of Mechanical Engineering, Pennsylvania State University, University Park, PA 16802

² Department of Engineering Science and Mechanics, Pennsylvania State University, University Park, PA 16802

I. INTRODUCTION

Controlling the propagation of surface waves in elastic media has numerous applications at different length scales, from seismic events to surface acoustic wave devices. Early studies investigated the attenuation of surface waves at both high [1] and low frequencies [2] using the concept of Phononic Crystals (PCs). PCs are periodic structures whose behavior is described by Bragg scattering, which requires lattice periodicity on the order of incident wave wavelength [3], [4]. In contrast, Locally Resonant Metasurfaces (LRMSs) allow sub-wavelength local resonators, as their working mechanism relies on the hybridization of the propagating wave with the resonators, making them suitable for low-frequency applications. In this paper, we present a novel strategy to tailor the dynamic response of LRMSs through a systematic design of their constituent local resonators.

Our approach to resonator design relies on manipulating its antiresonances to shape the frequency bandgap. Resonance frequencies represent a maximum displacement response upon dynamic excitations. In contrast, antiresonance frequencies represent an effective zero displacement in a specific direction (e.g., vertical or horizontal) subject to specific dynamic forces [5]. Following studies on plate waves [5], [6], the concept of resonances and antiresonances in generating and shaping the surface wave bandgaps has been well-established in numerical [7]–[9] and analytical studies [10], [11] since resonance and antiresonance frequencies, respectively, determine the start and end of a surface wave bandgap [7], [9]. The calculation of resonance frequencies for a resonator mounted over a half-space in the path of Rayleigh wave propagation does not appear in most of the earlier analytical studies based on the homogenization approach [10], [12]; their analytical estimation is challenging even for simple spring-mass systems [14] Thus, most of the metasurface studies resort to performing extensive dispersion analyses to create or enhance frequency bandgaps by varying the geometrical features of local resonators [13]–[16], typically considering mass-spring systems [17]–[20], prismatic resonators

[6], [21]–[24], or other simple geometries [25]–[27]. Recently, design optimization and machine learning methods have been used to propose more complex designs for LRMSs [28]–[32] mostly relying on creating bandgaps from dispersion analyses; however, our approach considers the fundamental physical interactions between resonators and the waveguide described by resonances and antiresonances, and how these interactions define frequency bandgaps.

Design of local resonators to compose LRMSs given target frequency bandgaps was proposed in our most recent works, a design strategy based on exploiting the resonators' antiresonances to obtain frequency bandgaps for plate [33] and surface waves [9], closely following our understanding of how these waves interact with displacement constraints applied to the waveguide's surface by local resonators [8]. Recently, we proposed a systematic design methodology to devise local resonators for LRMSs by matching their antiresonances with target frequencies [34]. This methodology enables the design of resonators without the need for coupling them to the waveguide's surface, as the resonators' antiresonance frequencies are the same when they are either loaded with unidirectional harmonic forces or with full plate wave motion [9]. This design strategy was successfully implemented in a case study of suppressing low-frequency S_0 Lamb wave mode in a thin plate [35] considering only the inplane motion of this particular Lamb wave mode; however, in the case of surface waves, the in-plane and the out-of-plane motion lead to different frequency bandgaps; therefore controlling both longitudinal-like and flexural-like antiresonances is the key to generating optimized resonators for LRMSs to prevent the propagation of Rayleigh waves.

In this paper, we present a systematic design methodology using Topology Optimization (TO) to design resonators for locally resonant metasurfaces by manipulating both longitudinal-like and flexural-like antiresonances, specifically targeting the two motion components of surface waves to generate frequency bandgaps for Rayleigh waves. TO has been used for decades to design elastic metamaterials initially considering design objectives such as negative Poisson's ratio [36] or extreme bulk modulus [37]; however, the introduction of TO in designing elastodynamic metamaterials for surface waves is an emerging research field, with the recent work focused on optimizing bandgaps from dispersion analyses of two-dimensional unit cells for plate waves [28], [30], [38] or surface waves [29], [39], mostly using genetic algorithms. In contrast, we present in this paper a three-dimensional density-based and gradient-based TO approach that tailors the local resonators' dynamic response without imposing periodicity conditions or having to compute dispersion analyses, which are particularly expensive for the case of surface waves due to their simulation complexity when modeling a full half-space.

The rest of the paper is organized in three sections. The topology optimization problem is introduced in Section 2, with three case studies illustrating the generation of bandgaps by manipulating antiresonances subject to different surface wave motion components. The experimental procedure is presented in Section 3 to validate the numerical results obtained with one of the optimized solutions, followed by our conclusions in Section 4.

II. TOPOLOGY OPTIMIZATION OF LOCAL RESONATORS

Surface waves' displacement motion in linear elastic media is described by an elliptical motion consisting of in-plane and out-of-plane components. Controlling these two components is the key to designing an effective resonator to prevent the propagation of surface waves using LRMSs as each component results in frequency bandgaps when antiresonances occur at the contact surface between the resonator and the waveguide. The design problem is then how to conceive a resonator that exhibits antiresonances for both in-plane and out-of-plane motion at designer-specified target frequencies. In this section, we present a TO design approach to match antiresonances with predefined target frequencies for each of the surface motion components, along with a discussion of three numerical case studies. The foundations of this optimization methodology have been presented in our preceding publication; please refer to [34] for details about the antiresonance matching approach using TO. Additionally, the optimization code can be downloaded in the following GitHub repository: https://github.com/danielgiraldoguzman/TopOpt EigenMatch

A. Optimization problem

The topology optimization problem is to systematically modify the material distribution within the design domain to minimize the objective function. In this approach, the objective function is defined such that the resonator's dynamic response exhibits antiresonances that match two predefined target frequencies. The first antiresonance mode targets the out-of-plane displacement component of surface waves, and the second the in-plane component. To simplify the resonator design, the surface wave motion is replaced by harmonic forces applied along in-plane and out-of-plane directions at the points where the resonator would contact the surface. Thus, the optimization problem is simplified to designing an individual resonator subject to two harmonic forces, as opposed to designing a complete metasurface subject to surface wave motion, effectively reducing the optimization's computational

complexity. The objective function minimizes the normalized difference between the antiresonance eigenfrequencies and their respective target frequencies, as follows:

$$\min_{\mathbf{\rho}} \left[w_1 \left(\frac{f_{A_out} - f_{T_out}}{f_{T_out}} \right)^2 + w_2 \left(\frac{f_{A_in} - f_{T_in}}{f_{T_in}} \right)^2 \right]$$
 (1)

91 subject to:

$$V_{\min} \le \sum_{e=1}^{N_e} \rho_e V_e \le V_{\max}$$
 (2a)

$$0 < \rho_{\min} \le \rho_e \le 1$$

where f_{T_out} and f_{T_in} are the respective target frequencies for out-of-plane and in-plane components, f_{A_out} and f_{A_in} the antiresonance eigenfrequencies of the resonator being optimized for the out-of-plane and in-plane component, respectively, and w_1 and w_2 are the scalar weighting factors defining the relative importance of each term in Eq. (1). The material distribution problem is parameterized using relative element densities, an approach that has been used for decades in the TO literature [40]. In Eq. (2), ρ is the vector of design variables, namely element pseudo-densities, where ρ_e is the pseudo-density associated with finite element e, and ρ_{min} is a very small number near zero used to prevent numerical errors. The effective element volume is $\rho_e V_e$, and the total volume $\sum_{e=1}^{N_e} \rho_e V_e$ is bounded by the maximum and minimum volume limits, V_{max} and V_{min} , respectively. The optimization problem presented in Eq. (1) and Eq. (2) is based on eigenfrequency matching informed by harmonic analysis [34], requiring the solution of the generalized eigenvalue problem at each iteration:

$$\mathbf{K}\mathbf{\Phi} = \mathbf{\lambda}\mathbf{M}\mathbf{\Phi} \tag{3}$$

where $\pmb{\lambda}$ is the matrix of eigenvalues such that $\lambda_q=2\pi f_{Aq}$ is the q^{th} eigenvalue and f_{Aq} its 104 corresponding eigenfrequency, and Φ the matrix of eigenvectors. **K** and **M** are respectively the stiffness and mass matrices, modified by the design variables ρ_{e} such that:

105

106

115

$$\mathbf{K} = \sum_{e=1}^{N_e} \rho_e \left[\mathbf{k}_e \right] \tag{4a}$$

$$\mathbf{M} = \sum_{e=1}^{N_e} \rho_e \left[\mathbf{m}_e \right] \tag{4b}$$

- where \mathbf{k}_{e} and \mathbf{m}_{e} are the element-wise stiffness and mass matrices, respectively. Note from Eq. (2) 107 108 that the design variables ρ_e range from ρ_{min} to 1, resulting in finite elements with near zero stiffness 109 and mass for design values near zero, and elements with material properties of the solid material when $\rho_e=1$. The procedure to identify and select appropriate antiresonance eigenfrequencies f_{A_out} and 110 f_{A in} to be used in Eq. (1) is as follows (for additional details, please refer to [34]): 111
- 112 Compute antiresonance eigenvalues and eigenvectors by solving Eq. (3) subject to 113 displacement boundary conditions at the degrees of freedom where antiresonances are 114 sought.
 - Compute the structure's response to harmonic forces to identify antiresonances from the frequency response function.
- 117 Evaluate antiresonance metrics, i.e., antiresonance amplitude, bandwidth, prominence, 118 and proximity to the target frequency.
- Compare the harmonic displacement response field, at the frequency where an 119 120 antiresonance has been identified, against all eigenvector solutions using the Modal 121 Assurance Criterion (MAC).

• Select the highest MAC coefficient between the harmonic response and an eigenvector as
the antiresonance eigenmode to be used in Eq. (1).

124

125

126

127

128

129

130

131

132

133

134

135

136

137

138

139

140

141

142

143

The optimization problem is solved using the gradient-based Sequential Linear Programming (SLP) method, which requires the linearization of objective and constraint functions, namely, a sensitivity analysis. Since the optimization constraints are linear functions, the objective function is linearized with respect to each design variable ρ_e using first-order Tylor series, such that Eq. (1) simplifies to:

$$\min_{\rho} \left[\left(w_1 \frac{\left(f_{A_out} - f_{T_out} \right)}{4\pi^2 f_{A_out} f_{T_out}^2} \frac{\partial \lambda_{A_out}}{\partial \rho_e} + w_2 \frac{\left(f_{A_in} - f_{T_in} \right)}{4\pi^2 f_{A_in} f_{T_in}^2} \frac{\partial \lambda_{A_in}}{\partial \rho_e} \right) \rho_e \right]. \tag{5}$$

The main optimization program, i.e., sensitivities and SLP solver, runs on MATLAB, calling the ABAQUS solver at each iteration to evaluate the objective function. Every sensitivity term in Eq. (5) is computed with respect to the design variables ho_e in a parallel loop. The optimization problem presented in Eq. (1) and Eq. (2) can be generalized for any case requiring the manipulation of multiple antiresonances; in this case, designing resonators for locally resonant metasurfaces considering multiple antiresonances for different wave motion components offers a wide range of possibilities during the optimization set up, as different weighting coefficients and target frequencies can be selected by the designer according to the problem requirements. The remainder of this section presents three case studies to demonstrate the implications of matching either a single or multiple antiresonances, highlighting the need for matching antiresonances for both in-plane and out-of-plane motions to control surface waves. TABLE I lists the optimization's initial parameters used in the case studies. Two target antiresonance frequencies have been selected for each motion component in the frequency range of the experimental test, i.e., 10 to 80 kHz. The design domain dimensions have been defined, considering the material properties used in the experimental test, to ensure feasible optimization solutions. This design domain has been discretized with serendipity second-order finite elements, whose size of 0.7 mm is small enough to accurately represent frequencies up to 80 kHz. The optimization starting point is a homogenously distributed material at the maximum volume constraint, i.e., 30% of the material density ($\rho_e = 0.3$), however, to ensure the optimized topology physically connects to the surface, full-density material ($\rho_e = 1$) has been enforced as a solid non-design region at the bottom of the design domain. Although these volume constraints are not strictly necessary to solve the optimization problem, they offer stability to the optimization process and result in topologies that efficiently use the design space. Using this combination of initial parameters, the optimization routine takes 30 to 50 iterations to find a solution, with an iteration time of around 15 minutes. For additional information about the selection of initial optimization parameters and how they influence the optimization solution, please refer to [34].

TABLE I. Optimization initial parameters.

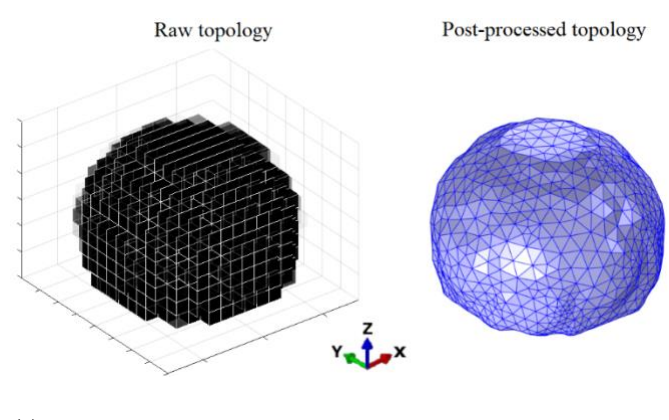
Target antiresonance	$f_{T_{ m out}} = 40~{ m kHz}$
frequencies	$f_{T_{\rm in}} = 30~{ m kHz}$
Material properties for topology-optimized resonators	$E = 3.9 \times 10^9 \mathrm{Pa}$ $\rho = 1214.65 \mathrm{kg/m^3}$ $v = 0.33$
Material properties for waveguide (half-space)	$E = 3.68 \times 10^9 \mathrm{Pa}$ $\rho = 1410 \mathrm{kg/m^3}$ $v = 0.332$
Design domain	14 × 14 × 14 mm

Mesh discretization	$20 \times 20 \times 20$ finite elements
Volume constraints	$V_{max} = 30\%$ $V_{min} = 10\%$
Starting point	Homogenous pseudo-density at $\rho_e=0.3$ Solid non-design 4 mm squared bottom base with void non-design surrounding elements.

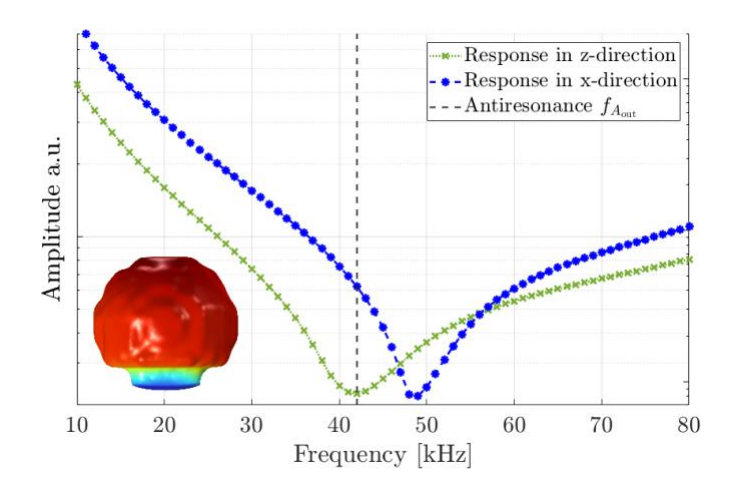
B. Single antiresonance matching

Frequency bandgaps for surface waves can be created by tailoring a single antiresonance subject to a load excitation in a particular direction; however, because of the elliptical motion of surface waves, another frequency bandgap may appear due to the other motion component not being controlled. In this subsection, this concept is illustrated via topology-optimized resonators obtained by varying the weighting coefficients \mathbf{w}_1 and \mathbf{w}_2 in Eq. (1), i.e., a single antiresonance mode for each of the motion components is tailored. Numerical analyses of the resulting optimized resonators' response to surface wave motion are presented.

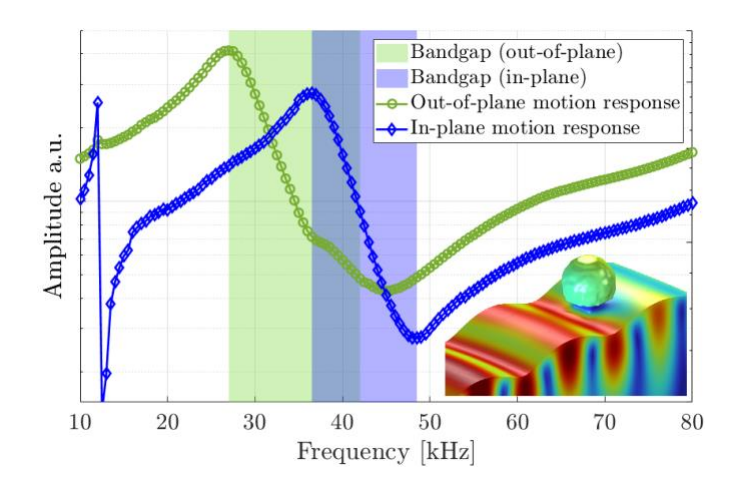
Case study #1: Consider the weighting coefficients $w_1 = 1$, and $w_2 = 0$ in Eq. (1), i.e., only the out-of-plane motion is considered by the optimizer, and all the other initial parameters as presented in TABLE I. The resultant topology and its corresponding analysis are presented in Fig. 1.



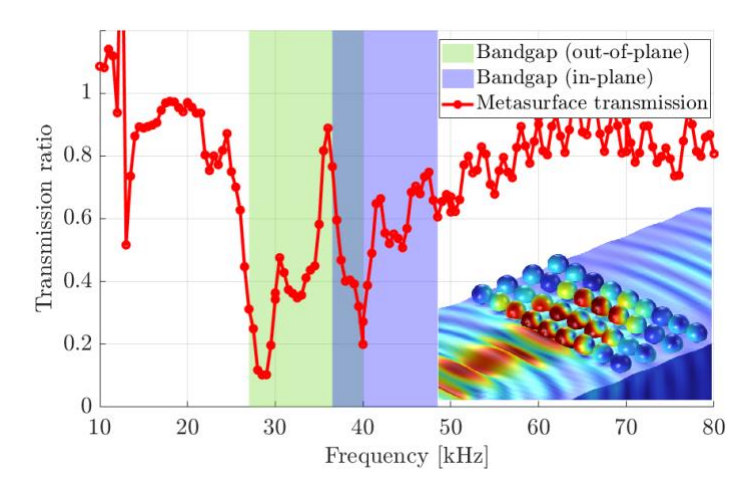
(a)



(b)



(c)



(d)

FIG. 1. (Color online). Case study #1 results. (a) Raw resultant topology with black and white voxels respectively for solid ($\rho_e = 1$) and void ($\rho_e = \rho_{min}$) material, and post-processed topology-optimized resonator meshed with tetrahedral elements in COMSOL Multiphysics®, (b) resonator's response to unidirectional harmonic forces in the x- or y-directions; inset shows a lateral view (xz plane) of the resonator's total displacement field subject to harmonic loads in the z-direction at 42 kHz, (c) frequency response to in-plane and out-of-plane surface wave motion components for a single resonator, inset shows a single resonator's total displacement field response to surface waves at 43 kHz, (d) surface wave transmission ratio for a metasurface composed of topology-optimized resonators, inset shows the metasurface's total displacement field response at 40 kHz. Note that frequency bandgaps for both the in-plane and out-of-plane components are depicted as shaded regions in subfigures (c) and (d). Insets of subfigures (b), (c), and (d) do not show absorption boundary regions for clarity, and they use the "Rainbow Classic" colormap from COMSOL Multiphysics®, with warm colors showing larger displacement values and cold colors representing relatively smaller displacement.

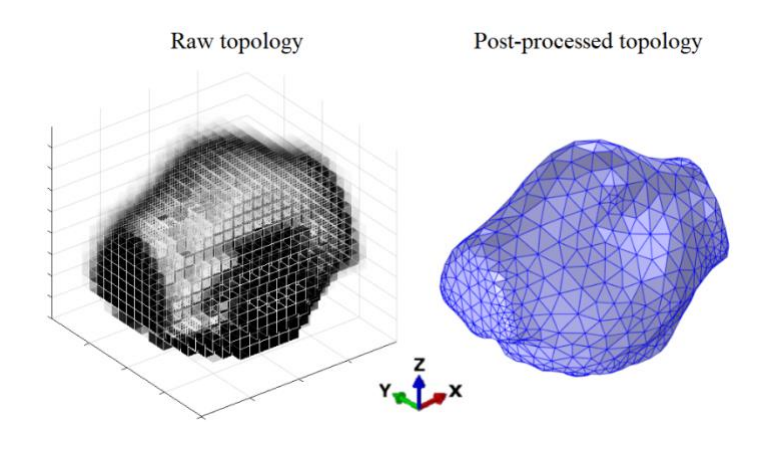
Figure 1 shows the resultant topology-optimized resonator for case study #1. This resonator exhibits an antiresonance due to harmonic forces in the z-direction close to the target frequency at 42 kHz (Fig. 1(b)). Another antiresonance due to harmonic forces in the x-direction occurs at 49 kHz; however, this antiresonance was not considered as an optimization goal since $w_2 = 0$ in Eq. (1). Once the resonator is mounted on a half-space and subject to Rayleigh waves, the antiresonance due to out-of-plane motion occurs at 43 kHz in Fig. 1(c), in accordance with the response to unidirectional harmonic forces in Fig. 1(b). The small frequency shift is the consequence of the complete surface wave motion interacting with this antiresonance mode, being influenced by the in-plane motion. The

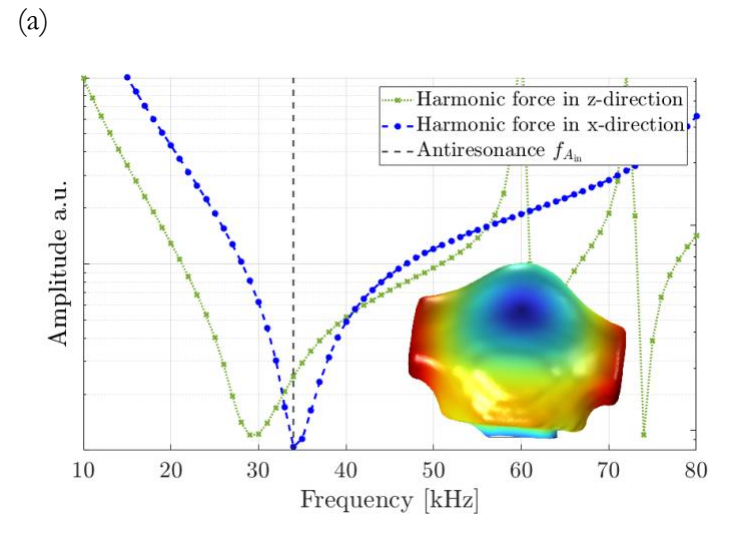
antiresonance due to in-plane motion, although not considered during the optimization process, happens to be at 48.5 kHz. Two frequency bandgaps develop once a locally resonant metasurface is arranged using these optimized resonators; each bandgap corresponds to out-of-plane and in-plane motion. Following [7], the bandgaps' bounds are defined from resonance to antiresonance in the frequency response to surface wave motion (Fig. 1(c)), depicted as shaded regions in Fig. 1(c)(d), respectively, from 27 kHz to 40 kHz for out-of-plane motion, and from 36.5 kHz to 48.5 kHz for in-plane motion. In Fig. 1(d), the maximum transmission loss for each bandgap is observed at 28.5 kHz and 40 kHz, respectively with transmission coefficients of 0.10 and 0.19. However, the overlap between the in-plane and out-of-plane bandgaps creates a transitional response splitting the two bandgaps, allowing the transmission of waves through the metasurface in this overlapping range with a peak transmission coefficient of 0.88 at 36 kHz.

- Figure 1(d), Fig. 2(d), and Fig. 3(d) present transmission loss plots of Rayleigh waves as a function of frequency when the resonators have been placed over the half-space's surface. These transmission ratio coefficients are computed as follows:
 - Run a baseline simulation of Rayleigh wave propagation in half-space for all frequencies of interest with no resonators placed on the surface.
 - Run the same simulation after mounting the optimized resonators over the half-space's surface, constituting the locally resonant metasurface.
 - Extract real and imaginary components of displacement at 15000 equally-spaced points over the half-space surface in the transmission region, i.e., after the metasurface region along the wave propagation direction. Extract the displacements at the same data points for both the baseline and the metasurface simulations.

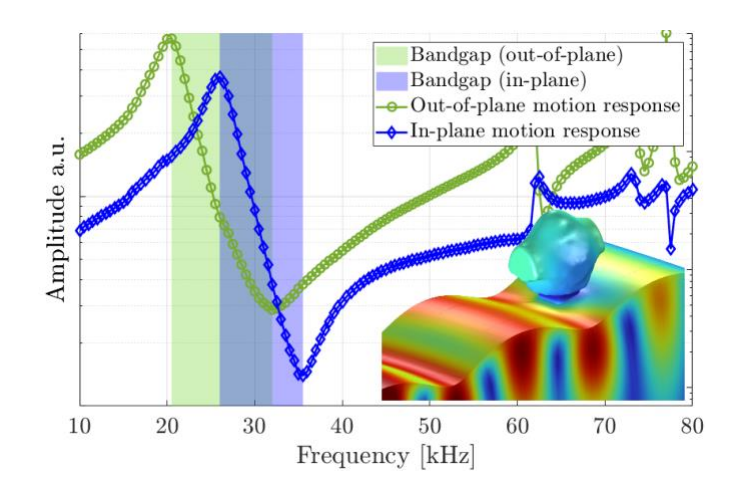
- Compute wavenumber spectra by performing 2D FFT (Fast Fourier transform) of the extracted displacements at each frequency, for both the baseline and metasurface simulations.
- Compute the transmission coefficients as the ratio between the maximum spectral amplitude of the metasurface and the baseline simulations, for each frequency.

Case study #2: Now consider the opposite weighting coefficients, i.e., $w_1 = 0$, and $w_2 = 1$ in Eq. (1), i.e., only the in-plane motion is considered by the optimizer, and all the other initial parameters as presented in TABLE I. The resultant topology and its corresponding analysis are presented in Fig. 2.





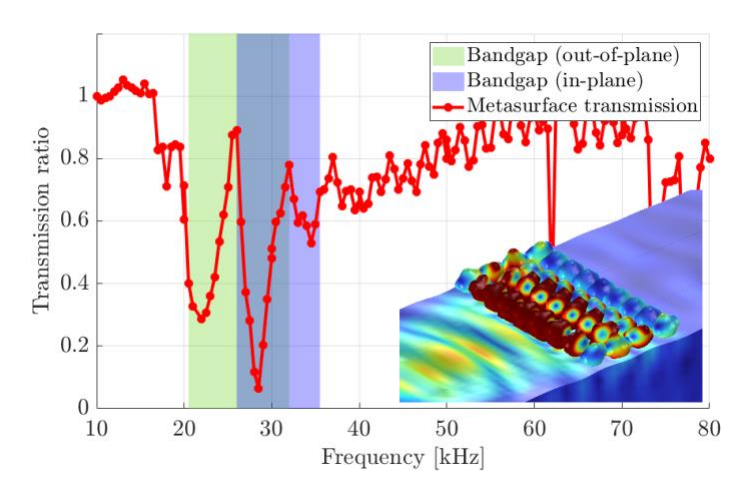
236 (b)



238

237

(c)



239

241

242

243

244

245

246

247

248

240 (d)

FIG. 2. (Color online). Case study #2. (a) Raw resultant topology with black and white voxels respectively for solid ($ho_e=1$) and void ($ho_e=
ho_{min}$) material, and post-processed topology-optimized resonator meshed with tetrahedral elements in COMSOL Multiphysics®, (b) resonator's response to unidirectional harmonic forces in the x- or y-directions; inset shows a lateral view (xz plane) of the resonator's total displacement field subject to harmonic loads in the x-direction at 34 kHz, (c) frequency response to in-plane and out-of-plane surface wave motion components for a single resonator, inset shows a single resonator's total displacement field response to surface waves at 35.5 kHz (d) surface wave transmission ratio for a metasurface composed of topology-optimized

resonators, inset show the metasurface's total displacement field response at 28.5 kHz. Note that frequency bandgaps for both the in-plane and out-of-plane components are depicted as shaded regions in subfigures (c) and (d). Insets of subfigures (b), (c), and (d) do not show absorption boundary regions for clarity, and they use the "Rainbow Classic" colormap from COMSOL Multiphysics®, with warm colors showing larger displacement values and cold colors representing relatively smaller displacement.

255

256

257

258

259

260

261

262

263

264

265

266

267

268

269

270

271

272

249

250

251

252

253

254

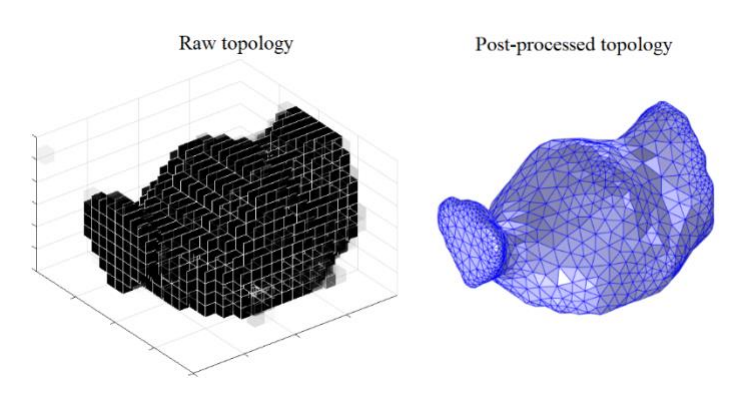
Similar to Case Study #1, Fig. 2 shows a topology-optimized resonator designed to exhibit an antiresonance due to unidirectional harmonic forces, this time along the x-direction with a target frequency $f_{T_{\rm in}} = 30$ kHz; however, in this case, the antiresonance has shifted to 34 kHz after postprocessing but the reason is not fully understood as a higher mesh discretization does not prevent this problem. Our optimization uses the ABAQUS solver with serendipity second-order (20-node) hexahedral elements to compute the objective function and evaluate sensitivities; however, the resultant post-processed topology is evaluated in COMSOL using second-order Lagrange tetrahedral elements. As different elements experience different levels of shear-locking, using these two different solvers with two different finite elements may explain the frequency shift observed for flexural-like modes. The antiresonance due to loads in the z-direction occurs at 29.5 kHz; note this frequency was not considered as an optimization objective since $w_1 = 0$ in Eq. (1). Once the resonator is mounted over the half-space under Rayleigh wave propagation, the antiresonance due to in-plane wave motion occurs at 35.5 kHz, as shown in Fig. 2(c), close to the antiresonance frequency under horizontal forced excitation (34 kHz), while the antiresonance due to out-of-plane motion appears at 32 kHz. Thus, two frequency bandgaps are expected from 26 kHz to 35.5 kHz and from 20.5 kHz to 32 kHz, respectively for in-plane and out-of-plane motion. In Fig. 2(d), the maximum transmission loss

for each bandgap is achieved at 22 kHz and 28.5 kHz, respectively with transmission ratio coefficients of 0.28 and 0.06. Similar to Case Study #1, the two bandgaps are not joined but divided by the resonance mode due to the in-plane motion happening, in this case, with a transmission coefficient of 0.89 at 26 kHz, as shown in Fig. 2(d).

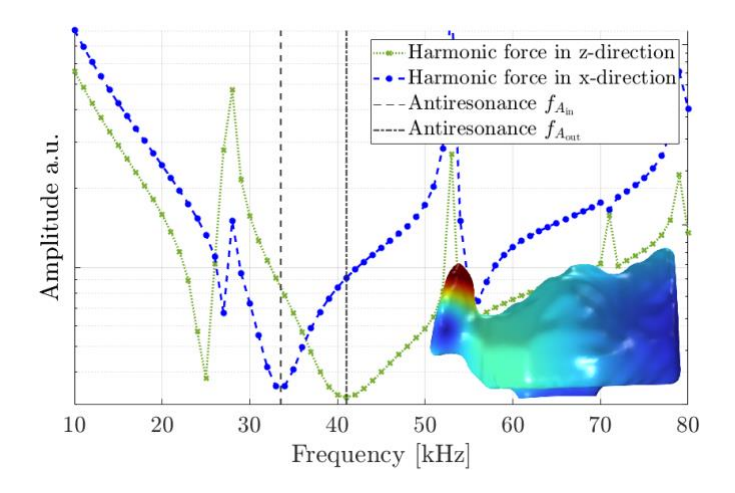
C. Double antiresonance matching

Matching a single antiresonance is useful to generate frequency bandgaps, however, as shown in case studies #1 and #2, the overlapping of in-plane and out-of-plane bandgaps allows the transmission of waves at their intersection. A double antiresonance matching approach offers control over both the out-of-plane and in-plane antiresonance modes. This subsection presents a case study that, contrary to the previous case studies, optimizes a resonator to exhibit two antiresonances at specific target frequencies, forcing the antiresonance due to in-plane motion to be lower than that due to out-of-plane motion. As will be demonstrated below, this approach reduces those undesired interactions, effectively removing the transitional response and combining the two bandgaps into a single wider bandgap.

Case study #3: Consider equal weighting coefficients $w_1 = 1$, and $w_2 = 1$ in Eq. (1), and all the other initial parameters as listed in TABLE I, i.e., both the in-plane and out-of-plane motions are considered by the optimizer. Fig. 3 shows the resultant topology-optimized resonator and its corresponding analysis of results.



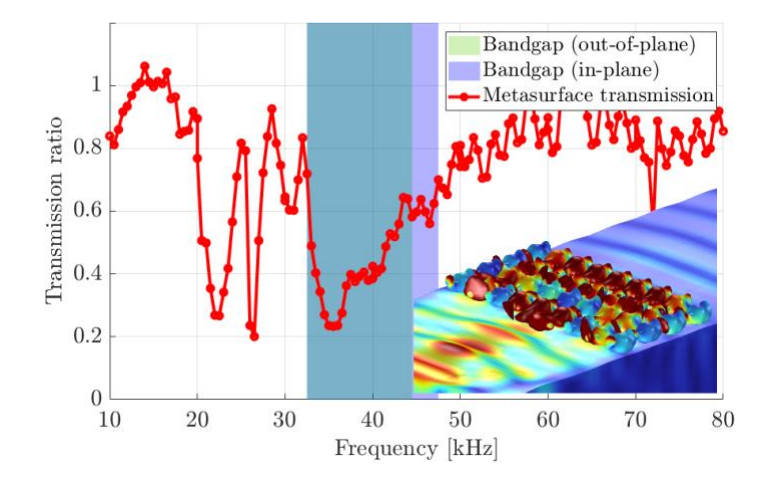
294 (a)



(b)

Bandgap (out-of-plane)
Bandgap (in-plane)
Out-of-plane motion response
In-plane motion response
Frequency [kHz]

(c)



(d)

FIG. 3. (Color online). Case study #3 analysis. (a) Raw resultant topology with black and white voxels respectively for solid ($\rho_e = 1$) and void ($\rho_e = \rho_{min}$) material, and post-processed topology-optimized resonator meshed with tetrahedral elements in COMSOL Multiphysics®, (b) resonator's response to unidirectional harmonic forces in the x- or y-directions; inset shows a lateral view (xz plane) of the resonator's total displacement field subject to harmonic loads in the z-direction at 41 kHz, (c) frequency response to in-plane and out-of-plane surface wave motion components for a single resonator; inset shows a single resonator's total displacement field response to surface waves at 44.5 kHz, (d) surface wave transmission ratio for a metasurface composed of topology-optimized resonators; inset shows the metasurface's total displacement field response at 35 kHz. Note that frequency bandgaps for both the in-plane and out-of-plane components are depicted as shaded regions in subfigures (c) and (d). Insets of subfigures (b), (c), and (d) do not show absorption boundary regions for clarity, and they use the "Rainbow Classic" colormap from COMSOL Multiphysics®, with warm colors showing larger displacement values and cold colors representing relatively smaller displacement.

Figure 3 presents the topology-optimized resonator designed by matching two antiresonances due to harmonic forces in the *x*- and *z*-directions. The antiresonances occur at 41 kHz in the *z*-direction and 33 kHz in the *x*-direction, as shown in Fig. 3(b). When the resonator is subject to Rayleigh waves, the antiresonance due to out-of-plane motion occurs at 44.5 kHz. The response to in-plane motion does not exhibit a clear antiresonance; a flat response is observed from 43 kHz to 51 kHz, nonetheless, the lowest amplitude is registered at 47.5 kHz. Thus, the two respective bandgaps for out-of-plane and in-plane motion extend from 32.5 kHz to 44.5 kHz and from 32.5 kHz to 47.5 kHz. Note that both bandgaps start at the same frequency because the resonance peak for both motion

components occurs at 32.5 kHz, as shown in Fig. 3(c). Moreover, the antiresonances for both components also happen in the same frequency range. This combination of resonances and antiresonances creates a single, wider bandgap, preventing the generation of undesired transitional responses and separation of bandgaps, as observed in case studies #1 and #2. In Fig. 3(d), the transmission coefficient at 35 kHz is 0.23, marking the lowest transmission point within the bandgap, however, by combining the effects of in-plane and out-of-plane motion, the resultant bandgap develops from 32.5 kHz to 47.5 kHz, which is a single and wider bandgap than those obtained in case studies #1 and #2. In the subsequent section, we present the experimental validation of the transmission loss for this case study.

All topology-optimized resonators presented in Fig. 1, Fig. 2, and Fig. 3, are the resultant topologies after the optimization process convergence, i.e., the objective function defined in Eq. (1) has reached a local minimum. TABLE II summarizes and compares the optimization results for each of the case studies. Note that these topologies have been obtained using the initial parameters presented in TABLE I; adjustments to these parameters might result in different solutions. Design domain dimensions, material properties, and frequency range must be appropriately defined to ensure feasible solutions. For additional case studies and analyses on how different optimization parameters may influence the solution, please refer to [34]. Finally, the optimized topologies have been arranged in a 9x4 regular grid to constitute a locally resonant metasurface as shown in the insets of Fig. 1(d), Fig. 2(d), and Fig. 3(d). This arrangement has not been optimized, meaning that other configurations of resonator placements will generate different results.

348 TABLE II Summary of results.

Case study	#1	#2	#3	
Weighting coefficients	$w_1 = 1$	$w_1 = 0$	$w_1 = 1$	
	$w_2 = 0$	$w_2 = 1$	$w_2 = 1$	
Target antiresonance	$f_{T \text{ out}} = 40 \text{ kHz}$	$f_{T_{ m lin}}=30~{ m kHz}$	$f_{T_{ m out}} = 40 \text{ kHz}$	
frequencies	71_out To MIL		$f_{T_{\rm in}} = 30 \; \mathrm{kHz}$	
Optimized			$f_{T_{-} \text{out}} = 41 \text{ kHz}$	
antiresonance	$f_{T_{-}\text{out}} = 42 \text{ kHz}$	$f_{T_{\mathrm{in}}} = 34 \mathrm{~kHz}$	$f_{T_{ m in}} = 33~{ m kHz}$	
frequencies			-	
Bandgap (out-of-plane)	27 - 40 kHz	26 - 35.5 kHz	32.5 - 47.5 kHz.	
Bandgap (in-plane)	36.5 - 48.5 kHz	20.5 - $32~\mathrm{kHz}$	32.3 - 47.3 KHZ.	
Transmission	0.10 at 28.5 kHz	0.28 at 22 kHz		
coefficients;	0.19 at 40 kHz	0.06 at 28.5 kHz	0.23 at 35 kHz	
lowest within bandgap				
Transmission			No transitional	
coefficients;	0.89 at 26 kHz	0.88 at 36 kHz	response	
transitional peak			•	

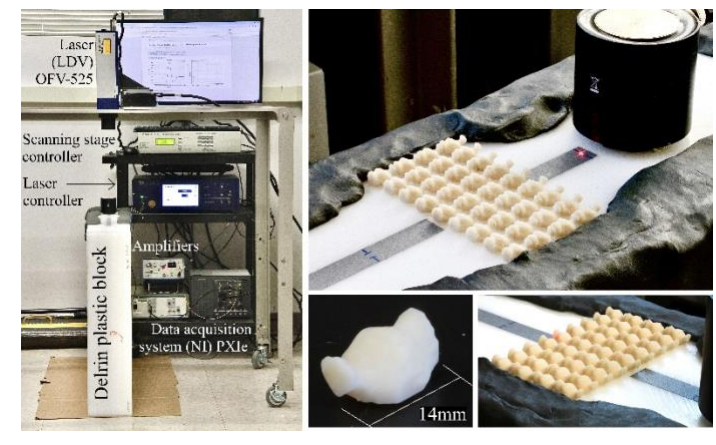
III. EXPERIMENTAL VALIDATION OF CASE STUDY #3

D. Experimental setup

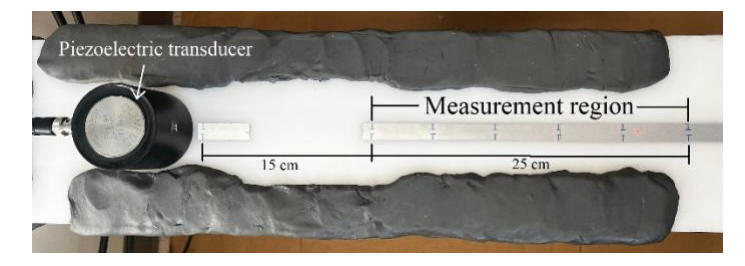
Surface wave experiments are performed on a Delrin plastic block of dimensions 914×152×635 mm (36×6×25 inches) with material properties (Young's modulus = 3.68 GPa, density = 1410 kg/m³, Poisson's coefficient 0.332) estimated from wave speed measurements. The experimental setup comprises a National Instruments (NI) data acquisition system with arbitrary waveform generator PXIe-5433 and oscilloscope PXIe-5172 cards, a TEGAM amplifier set up to 50x amplification factor, an Olympus pre-amplifier set up to a 25dB gain, and a scanning laser setup equipped with a long-range PSV-505 Laser Doppler Vibrometer (LDV) mounted on a 250 mm scan length micro-precision Newport scanning stage ILS250PP and controller ESP301, with the laser pointing at a reflective tape on the block's surface to measure the out-of-plane particle velocity at multiple points, as shown in Fig. 4(a). A 100-kHz P-wave Olympus transducer is glued to the narrow side of the plastic block, i.e., to the face with dimensions 914×152 mm (36×6 inches), thus separating the compressional waves reflecting from the back wall from the surface waves. Moreover, to minimize reflections from side walls, a duct seal is applied on both edges of the testing surface, as shown in Fig. 4. We employed two broadband Ricker waveforms with, respectively, 30 kHz and 50 kHz central frequencies to fully cover the frequency range under study.

The topology-optimized resonator of Case Study #3 (Fig. 3) is selected for experimental validation as it was obtained by optimizing antiresonances for both the in-plane and out-of-plane surface wave motion components. This resonator has been 3D printed using Stereolithography (SLA) with material properties (density = 1214.65 kg/m³, Young's modulus = 3.9 GPa, and Poisson's coefficient = 0.33) measured from resonance ultrasonic measurements. An arrangement of 28 printed resonators is glued

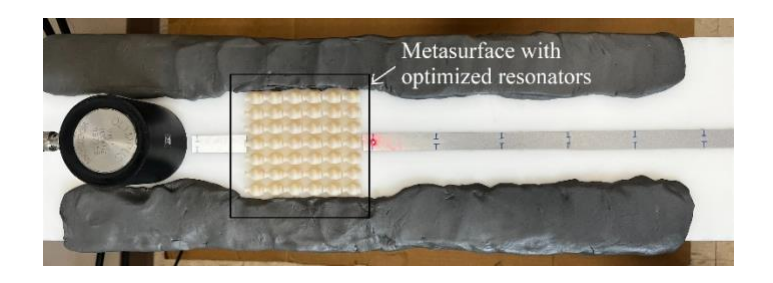
on the Delrin block's surface in a regular grid configuration to compose the locally resonant metasurface; the same arrangement is used in the numerical studies of Fig 3. The out-of-plane velocity is captured with a 50 MHz sampling frequency for 51 points after the metasurface (starting at 15 cm from the piezoelectric transducer) along the wave propagation direction in scanning steps of 5 mm; sufficient to identify wave modes propagating at wavenumbers up to 600 rad/m. We perform two independent experiments using the two excitation Ricker waveforms at 30kHz and 50kHz: (i) baseline (without resonators) and (ii) metasurface (with an array of resonators), while keeping all the other experimental conditions the same. To verify the generated signal amplitudes in each test are consistent, the back-wall reflection wave is used as a reference as this wave bounces back from the block's bottom surface, therefore not being affected by the metasurface presence.



386 (a)



388 (b)



(c)

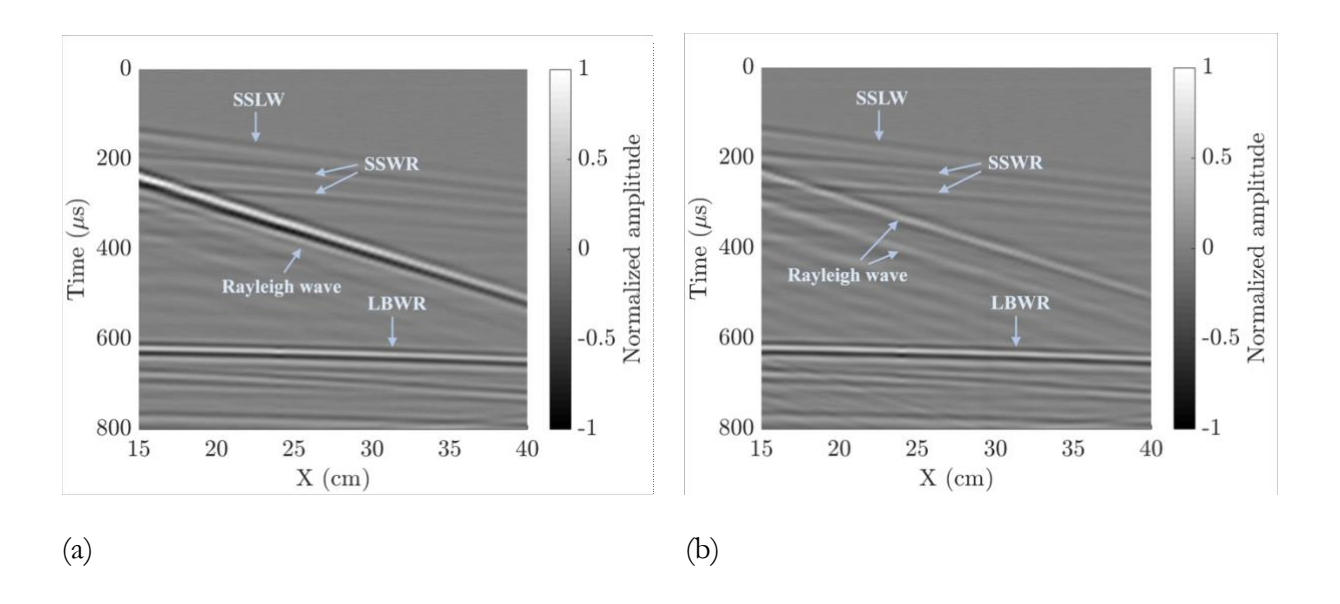
FIG. 4. (Color online). Experimental setup. (a) Collage of photos showing the laser (LDV) pointing at the block's surface, and close-up photos of the locally resonant metasurface composed of 3D-printed optimized resonators from Case study #3. (b) Baseline and (c) metasurface measurement configurations.

E. Experimental results

Waterfall plots (B-scans) in the absence and presence of the metasurface are compared in Fig. 5 for the test performed with the 30 kHz Ricker wavelet excitation. Four distinct wave packets can be observed in the baseline waterfall plot: (i) surface skimming longitudinal waves (SSLW), (ii) surface sidewall reflections (SSWR), (iii) Rayleigh waves, and (iv) longitudinal back-wall reflections (LBWR), as marked in Fig. 5(a)(b). As expected, Rayleigh wave amplitude attenuation in the presence of the metasurface is observed in the waterfall plots. However, it is difficult to quantify the attenuation at different frequencies just relying on the time-domain signals. Thus, we construct wavenumber-frequency dispersion spectra by performing 2D FFT over the waterfall data to visualize different wave modes propagating at distinct frequencies along the scanning path. Note that to exclude the LBWR from all subsequent results, we have limited the analysis to data contained in the first 575 μ s (Fig. 5 (a)(b)) for both baseline and metasurface measurements.

The dispersion spectrum for the baseline plot, Fig. 5(c), indicates the presence of Rayleigh wave modes with a strong signal amplitude spanning from 15 kHz to 60 kHz. On the other hand, for the metasurface configuration, in Fig. 5(d), we can observe two splits in the spectral amplitude signature, indicating the formation of bandgaps due to the metasurface presence. It should be noted that waterfall plots are normalized against the corresponding maxima in the baseline measurement. The wave transmission is then estimated by taking the ratio between the maximum spectral amplitude of the metasurface and baseline configurations over the desired frequency range (dashed white lines in Fig. 5(c)(d)). To remove potential influence of non-surface wave modes, the maximum spectral amplitude is taken within a range of ± 25 rad/m around the expected Rayleigh wave dispersion line; both limits are marked as solid light green lines in Fig. 5 (c)(d).





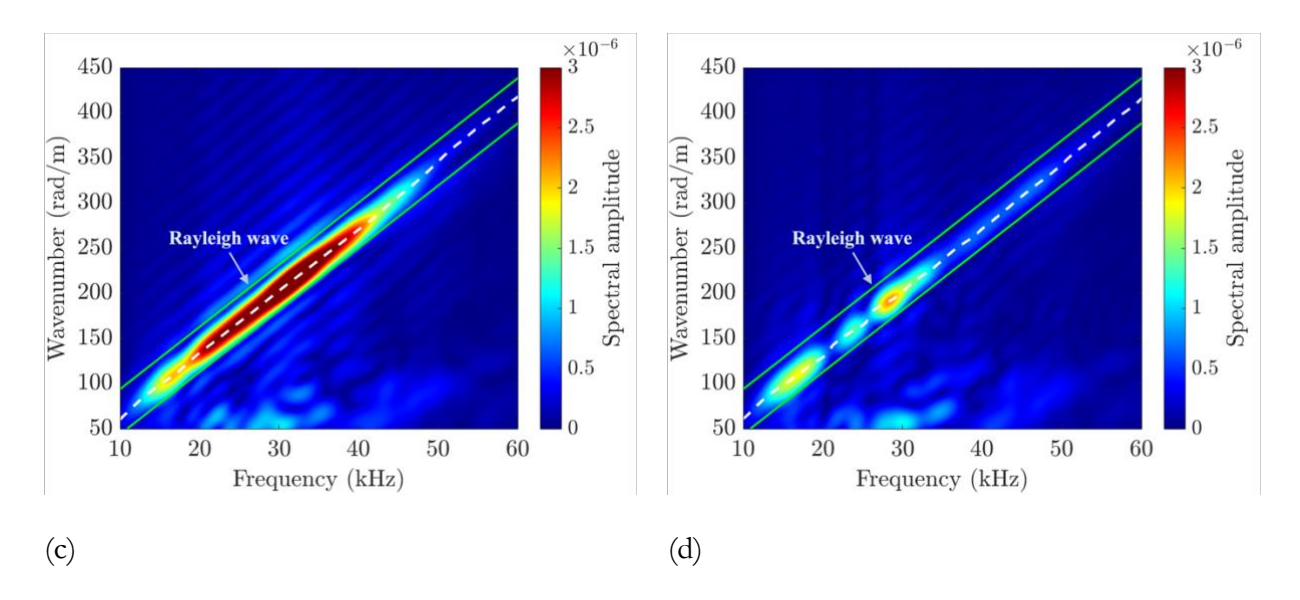


FIG. 5. (Color online). Experimental measurement results as waterfall plots and their respective wavenumber-frequency dispersion spectra. Following the experimental configurations shown in Fig. 4, (a) and (c) are baseline measurements, (b) and (d) are metasurface measurements.

The experimentally-estimated spectral transmission ratio, using both the 30 kHz and 50 kHz excitations, are shown in Fig. 6. Despite performing two independent experiments, both transmission ratio plots agree well over the desired frequency range (20 – 70 kHz), thereby validating the experimental procedures and the data analysis strategy used in deriving the transmission ratio for both the numerical and experimental results. The experimental spectral transmission plots correlate well with the numerical results, i.e., the predicted bandgap from 32.5 kHz to 47.5 kHz by the numerical analysis is observed in the experimental test, demonstrating the practical feasibility of the proposed topology optimization strategy in designing metasurfaces to suppress surface waves.

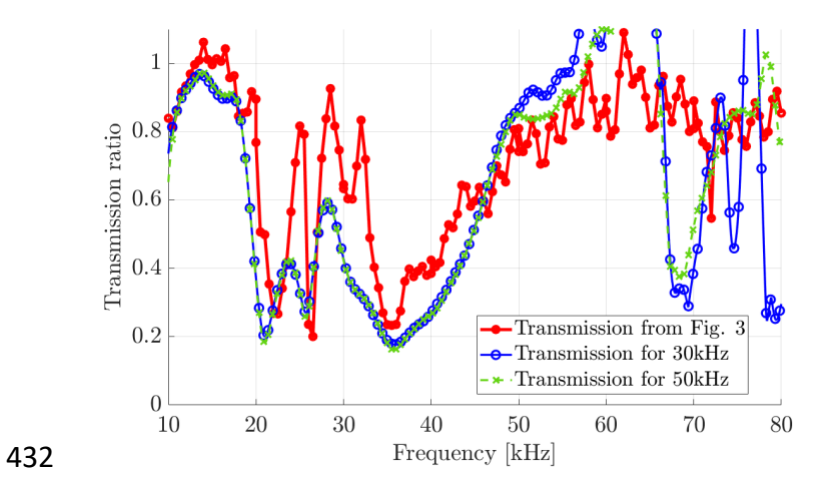


FIG. 6. (Color online). Comparison of numerical and experimental transmission plots. Numerical transmission plot from Fig. 3(d) (red solid line with circular markers) and transmission plots from experimental results using two independent Ricker wave excitations with center frequencies 30 kHz (blue solid line with circular markers) and 50 kHz (green dashed line with cross markers).

IV. SUMMARY AND CONCLUSION

The design of locally resonant metasurfaces to prevent the propagation of surface waves can be simplified to designing an isolated local resonator by tailoring its antiresonances subject to unidirectional harmonic forces applied at the location where the resonator would connect to the surface. Since the particle displacement profile of surface waves is described by an elliptical motion, these antiresonances must be obtained by individually applying both in-plane and out-of-plane harmonic forces. This is because each component of surface motion leads to a different frequency bandgap; therefore, failing to control one of the two bandgaps could result in an undesired response, as was exemplified in case studies #1 and #2. Specifically, an overlap between the two bandgaps results in significant transmission at the frequency range where both bandgaps intersect. Thus, appropriate manipulation of each bandgap is the key to obtaining wider frequency bandgaps.

When designing a local resonator that generates two overlapping bandgaps, tailoring its antiresonances to appropriate frequencies is crucial to ensure the fully overlapping instead of multiple separated bandgaps. In this paper, we presented three case studies to illustrate the separation w combination of bandgaps, given specific antiresonance target frequencies. When a single antiresonance is controlled (Case studies #1 and #2), either the in-plane or out-of-plane component, the out-of-plane antiresonance seems to appear at a lower frequency than the in-plane antiresonance and the resultant spectral transmission ratio exhibits a transitional response that occurs at the intersection of the two bandgaps, mainly because of a resonance happening in this range, as shown in Fig. 1(c) and Fig. 2(c). An effective approach to prevent this transitional response, and therefore obtain a single wider bandgap, is to manipulate the order in which these antiresonances occur, i.e., making the in-plane component antiresonance occur at a lower frequency than that corresponding to the out-of-plane component. This manipulation results in an effective design approach to combine frequency bandgaps

as demonstrated by case study #3. Numerical and experimental results pertaining to case study #3 show excellent agreement; the expected bandgaps from the numerical analyses have been observed in the experimental results, specifically by comparing spectral transmission ratio plots.

This paper demonstrates a systematic design methodology to conceive local resonators using topology optimization by matching antiresonance frequencies with specific targets. We present an effective methodology to create locally resonant metasurfaces composed of multiple optimized resonators with a wide bandgap occurring around the target frequencies. An antiresonance subject to harmonic forces correlates well with the antiresonance once the resonator is attached to the waveguide's surface, however, future studies are necessary to understand the resonances of local resonators in response to surface waves once they are attached to the waveguide. This is an important consideration since frequency bandgaps are bounded by resonances and antiresonances, therefore a fundamental understanding of how to predict the frequency at which the resonance occurs is required to design optimized topologies for surface wave propagation. Thus, a future design approach should consider controlling both resonances and antiresonances as the essential factor in generating wider bandgaps.

476	ACKNOWLEDGMENTS
477	This work was supported by the National Science Foundation under grant No.1934527. Any opinions,
478	findings, conclusions, or recommendations expressed in this material are those of the author(s)and do
479	not necessarily reflect the views of the National Science Foundation.
480	Computations for this research were performed on the Pennsylvania State University's Institute for
481	Computational and Data Sciences' Roar supercomputer.
182	The authors gratefully acknowledge Luke B. Beardslee from Los Alamos National Laboratory for his
483	support during our development of the experimental setup, and Dr. Guha Manogharan and Ankit
484	Saxena for their support with additive manufacturing of samples for this study.
485	
486	AUTHOR DECLARATIONS
487	Conflict of Interest: There is no conflict of interest to disclose.
488	
189	DATA AVAILABILITY
490	The data that support the findings of this study are available from the corresponding author upon
491	reasonable request.

492 REFERENCES

- 493 [1] N. Boechler, J. K. Eliason, A. Kumar, A. A. Maznev, K. A. Nelson, and N. Fang,
 494 "Interaction of a contact resonance of microspheres with surface acoustic waves," 2013. doi: 10.1103/PhysRevLett.111.036103.
- F. Meseguer *et al.*, "Two-dimensional elastic bandgap crystal to attenuate surface waves," *J. Light. Technol.*, vol. 17, no. 11, pp. 2196–2201, Nov. 1999, doi: 10.1109/50.803011.
- T. Lee and H. Iizuka, "Bragg scattering based acoustic topological transition controlled by local resonance," *Phys. Rev. B*, vol. 99, no. 6, p. 064305, Feb. 2019, doi: 10.1103/PHYSREVB.99.064305/FIGURES/8/MEDIUM.
- 501 [4] S. Brûlé, E. H. Javelaud, S. Enoch, and S. Guenneau, "Experiments on seismic metamaterials: Molding surface waves," *Phys. Rev. Lett.*, vol. 112, no. 13, pp. 1–5, 2014, doi: 10.1103/PhysRevLett.112.133901.
- E. G. Williams, P. Roux, M. Rupin, and W. A. Kuperman, "Theory of multiresonant metamaterials for A0 Lamb waves," *Phys. Rev. B Condens. Matter Mater. Phys.*, vol. 91, no. 10, pp. 1–12, 2015, doi: 10.1103/PhysRevB.91.104307.
- 507 [6] M. Rupin, F. Lemoult, G. Lerosey, and P. Roux, "Experimental demonstration of ordered 508 and disordered multiresonant metamaterials for lamb waves," *Phys. Rev. Lett.*, vol. 112, no. 23, 509 pp. 1–5, 2014, doi: 10.1103/PhysRevLett.112.234301.
- 510 [7] A. Colombi, P. Roux, S. Guenneau, P. Guéguen, and R. V. Craster, "Forests as a natural seismic metamaterial: Rayleigh wave bandgaps induced by local resonances," *Sci. Rep.*, vol. 6, no. January, pp. 1–7, 2016, doi: 10.1038/srep19238.
- 513 [8] L. S. S. Pillarisetti, C. J. Lissenden, and P. Shokouhi, "Control of Rayleigh wave propagation through imposing Mindlin boundary conditions on the surface," *J. Sound Vib.*, vol. 530, p. 116931, Jul. 2022, doi: 10.1016/J.JSV.2022.116931.
- 516 [9] L. S. S. Pillarisetti, C. J. Lissenden, and P. Shokouhi, "Understanding the role of resonances and anti-resonances in shaping surface-wave bandgaps for metasurfaces," *J. Appl. Phys.*, vol. 132, no. 16, p. 164901, Oct. 2022, doi: 10.1063/5.0093083.
- 519 [10] D. Colquitt, A. Colombi, R. V. Craster, P. Roux, and S. Guenneau, "Seismic metasurfaces: Sub-wavelength resonators and Rayleigh wave interaction," *J. Mech. Phys. Solids*, vol. 99, no. November 2016, pp. 379–393, 2017, doi: 10.1016/j.jmps.2016.12.004.
- 522 [11] X. Pu, A. Palermo, and A. Marzani, "Lamb's problem for a half-space coupled to a generic distribution of oscillators at the surface," *Int. J. Eng. Sci.*, vol. 168, no. March, p. 103547, 2021, doi: 10.1016/j.ijengsci.2021.103547.
- 525 [12] A. Palermo, S. Krödel, A. Marzani, and C. Daraio, "Engineered metabarrier as shield from seismic surface waves," *Sci. Rep.*, vol. 6, 2016, doi: 10.1038/srep39356.
- 527 [13] Z. Liu *et al.*, "Locally Resonant Sonic Materials," *Science (80-.).*, vol. 289, no. 5485, pp. 1734–
 528 1736, 2000, doi: 10.1126/science.289.5485.1734.
- [14] Q. Lin, J. Zhou, H. Pan, D. Xu, and G. Wen, "Numerical and Experimental Investigations on Tunable Low-frequency Locally Resonant Metamaterials," *Acta Mech. Solida Sin.*, vol. 34, no. 5, pp. 612–623, Oct. 2021, doi: 10.1007/S10338-021-00220-4/FIGURES/7.
- 532 [15] A. O. Krushynska, V. G. Kouznetsova, and M. G. D. Geers, "Towards optimal design of locally resonant acoustic metamaterials," *J. Mech. Phys. Solids*, vol. 71, pp. 179–196, Nov. 2014, doi: 10.1016/j.jmps.2014.07.004.
- 535 [16] M. Miniaci, A. Krushynska, F. Bosia, and N. M. Pugno, "Large scale mechanical metamaterials as seismic shields," *New J. Phys.*, vol. 18, no. 8, 2016, doi: 10.1088/1367-2630/18/8/083041.
- 538 [17] F. Zeighami, A. Palermo, and A. Marzani, "Rayleigh waves in locally resonant metamaterials,"

- 539 Int. J. Mech. Sci., vol. 195, no. December 2020, 2021, doi: 10.1016/j.ijmecsci.2020.106250.
- 540 [18] A. Palermo and A. Marzani, "Control of Love waves by resonant metasurfaces," *Sci. Rep.*, vol. 8, no. 1, pp. 1–8, 2018, doi: 10.1038/s41598-018-25503-8.
- 542 [19] R. Zaccherini *et al.*, "Locally Resonant Metasurfaces for Shear Waves in Granular Media," 543 *Phys. Rev. Appl.*, vol. 13, no. 3, p. 1, 2020, doi: 10.1103/PhysRevApplied.13.034055.
- 544 [20] C. Zeng, C. Zhao, and F. Zeighami, "Seismic surface wave attenuation by resonant
 545 metasurfaces on stratified soil," *Earthq. Eng. Struct. Dyn.*, vol. 51, no. 5, pp. 1201–1223, 2022,
 546 doi: 10.1002/eqe.3611.
- 547 [21] A. Colombi, D. Colquitt, P. Roux, S. Guenneau, and R. V. Craster, "A seismic metamaterial: The resonant metawedge," *Sci. Rep.*, vol. 6, no. Umr 7249, pp. 1–6, 2016, doi: 10.1038/srep27717.
- 550 [22] M. Lott, P. Roux, S. Garambois, P. Guéguen, and A. Colombi, "Evidence of metamaterial
 551 physics at the geophysics scale: The METAFORET experiment," *Geophys. J. Int.*, vol. 220, no.
 552 2, pp. 1330–1339, 2020, doi: 10.1093/gji/ggz528.
- C. Boutin, L. Schwan, and M. S. Dietz, "Elastodynamic metasurface: Depolarization of mechanical waves and time effects," *J. Appl. Phys.*, vol. 117, no. 6, p. 064902, Feb. 2015, doi: 10.1063/1.4908135.
- 556 [24] A. Colombi *et al.*, "Enhanced sensing and conversion of ultrasonic Rayleigh waves by elastic metasurfaces," *Sci. Reports 2017 71*, vol. 7, no. 1, pp. 1–9, Jul. 2017, doi: 10.1038/s41598-017-07151-6.
- 559 [25] Y.-C. Su and C.-K. Wu, "A snowman-like seismic metamaterial," *J. Appl. Phys.*, vol. 132, no. 10, p. 105106, Sep. 2022, doi: 10.1063/5.0098429.
- 561 [26] W. Liu, G. H. Yoon, B. Yi, Y. Yang, and Y. Chen, "Ultra-wide band gap metasurfaces for controlling seismic surface waves," *Extrem. Mech. Lett.*, vol. 41, p. 101018, Nov. 2020, doi: 10.1016/J.EML.2020.101018.
- Z. Chen, G. Wang, and C. W. Lim, "Artificially engineered metaconcrete with wide bandgap for seismic surface wave manipulation," *Eng. Struct.*, vol. 276, p. 115375, Feb. 2023, doi: 10.1016/J.ENGSTRUCT.2022.115375.
- Z. Liu, S. B. Shan, H. W. Dong, and L. Cheng, "Topologically customized and surface-mounted meta-devices for Lamb wave manipulation," *Smart Mater. Struct.*, vol. 31, no. 6, 2022, doi: 10.1088/1361-665X/ac64db.
- [29] Z. Liu, H. W. Dong, G. L. Yu, and L. Cheng, "Achieving ultra-broadband and ultra-low-frequency surface wave bandgaps in seismic metamaterials through topology optimization,"
 [70] Compos. Struct., vol. 295, p. 115863, Sep. 2022, doi: 10.1016/J.COMPSTRUCT.2022.115863.
- J. Jung, S. Goo, and J. Kook, "Design of a local resonator using topology optimization to tailor bandgaps in plate structures," *Mater. Des.*, vol. 191, p. 108627, Jun. 2020, doi: 10.1016/J.MATDES.2020.108627.
- 576 [31] X. Yang and Y. Y. Kim, "Topology optimization for the design of perfect mode-converting anisotropic elastic metamaterials," *Compos. Struct.*, vol. 201, no. April, pp. 161–177, 2018, doi: 10.1016/j.compstruct.2018.06.022.
- 579 [32] C. X. Liu and G. L. Yu, "Inverse design of locally resonant metabarrier by deep learning with
 580 a rule-based topology dataset," *Comput. Methods Appl. Mech. Eng.*, vol. 394, p. 114925, May
 581 2022, doi: 10.1016/J.CMA.2022.114925.
- [33] C. J. Lissenden, C. N. Hakoda, and P. Shokouhi, "Control of low-frequency Lamb wave propagation in plates by boundary condition manipulation," *J. Appl. Phys.*, vol. 129, no. 9, 2021, doi: 10.1063/5.0042576.
- D. Giraldo Guzman, C. Lissenden, P. Shokouhi, and M. Frecker, "Topology Optimization
 Design of Resonant Structures Based on Antiresonance Eigenfrequency Matching Informed

- 587 by Harmonic Analysis," J. Mech. Des. Trans. ASME, vol. 145, no. 10, Oct. 2023, doi: 10.1115/1.4062882/7025780/MD_145_10_101704.PDF.
- [35] D. Giraldo Guzman, L. S. S. Pillarisetti, S. Sridhar, C. J. Lissenden, M. Frecker, and P.
 Shokouhi, "Design of resonant elastodynamic metasurfaces to control S 0 Lamb waves using topology optimization," JASA Express Lett., vol. 2, no. 11, p. 115601, Nov. 2022, doi: 10.1121/10.0015123.
- [36] U. D. Larsen, O. Sigmund, and S. Bouwstra, "Design and fabrication of compliant micromechanisms and structures with negative Poisson's ratio," *J. Microelectromechanical Syst.*, vol. 6, no. 2, pp. 99–106, Jun. 1997, doi: 10.1109/84.585787.
- 596 [37] O. Sigmund, "A new class of extremal composites," J. Mech. Phys. Solids, vol. 48, no. 2, pp. 397–428, Feb. 2000, doi: 10.1016/S0022-5096(99)00034-4.
- 598 [38] S. Halkjær, O. Sigmund, and J. S. Jensen, "Maximizing band gaps in plate structures," *Struct. Multidiscip. Optim.*, vol. 32, no. 4, pp. 263–275, 2006, doi: 10.1007/s00158-006-0037-7.
- [39] Z. Liu, H. W. Dong, and G. L. Yu, "Topology optimization of periodic barriers for surface waves," *Struct. Multidiscip. Optim.*, vol. 63, no. 1, pp. 463–478, Jan. 2021, doi: 10.1007/S00158-020-02703-3/FIGURES/15.
- 603 [40] M. P. Bendsøe, A. Díaz, and N. Kikuchi, "Topology and Generalized Layout Optimization of
 604 Elastic Structures," *Topol. Des. Struct.*, pp. 159–205, 1993, doi: 10.1007/978-94-011-1804 605 0_13.